Model of Laminated Ferromagnetic Cores for Loss Prediction in Electrical Machines

Paavo Rasilo[1], Emad Dlala[1], Katarzyna Fonteyn[1], Jenni Pippuri[2], Anouar Belahcen[1], Antero Arkkio[1]
[1] Aalto University School of Electrical Engineering, Department of Electrical Engineering, P.O. Box 13000 FI-00076 Aalto, Finland
[2] VTT Electrical Product Concepts, FI-02044 VTT, Espoo, Finland
E-mail: paavo.rasilo@aalto.fi

Abstract

An iron-loss model for laminated ferromagnetic cores of electrical machines is presented and applied to estimate the core losses of an induction machine with finite element analysis. Skin effect in the cross section of the core lamination is modeled using a set of sinusoidal basis functions while locally considering both the hysteretic material properties and the excess field caused by domain wall motion. After spatial and time discretization, a single nonlinear equation system is obtained. An accurate vector Preisach model, the differential reluctivity tensor and the Newton-Raphson method guarantee excellent convergence of the iteration procedure. Results from the model correspond well to iron-loss data obtained by measurements.

1. Introduction

Two-dimensional finite element (FE) analysis is commonly used in design and analysis of electrical machines with laminated iron cores. One of the major simplifying assumptions of the 2-D model is that the eddy currents in the core regions are assumed to be zero and thus have no effect on the magnetic field to be calculated. Although this assumption may be reasonable for the axial component of the currents in thin laminations, the currents flowing parallel to the cross-sectional plane of the machine may have a damping effect on the inducing field, especially at higher frequencies. Thus a method to include the eddy-current effects into the field analysis is needed for accurate loss prediction of variable-speed drives in which high-frequency flux-density harmonics commonly occur.

In addition to traditionally omitting the eddy-current losses from the analysis, simplified single-valued or even linear material properties are often assumed in the calculation. However, since ferromagnetic lamination materials generally have hysteretic material properties, accurate modeling of electrical machines requires application of convenient history-dependent hysteresis models. The eddy-current distribution in the lamination cross-section is strongly dependent on the actual material properties, which requires also modeling the coupling between the eddy-current and hysteresis effects. In addition, the local excess eddy currents caused by the domain wall movement may need to be considered.

Several researchers have proposed methods to include the iron losses into the magnetic field calculation. In [1] this was implemented by assuming uniform flux-density distribution in the lamination cross section thus neglecting the skin effect. In [2],

a simplified model was presented to take into account the phase lag between the surface field strength and the average flux density without actually modeling the skin effect. These models are fast but their accuracy may be poor especially in thick lamination cases and at high frequencies which cause the skin effect to be significant. For instance the poles of large wound-field synchronous generators and motors are commonly stacked of 2 mm steel laminations to reduce the manufacturing costs. Due to the thickness and high conductivity of these sheets, significant eddy currents may be induced on the pole surface especially if the motor is driven by a frequency converter. To accurately study such cases by simulations, more detailed models are needed to account for the skin effect in the lamination.

In [3] and [4], the skin effect was modeled by a separate 1-D FE model coupled to the 2-D FE model through a nested iteration procedure. In [5], the 2-D and 1-D models were implemented as a single system of equations. The 2-D/1-D coupling results in a large number of unknowns and hence slows down the computation but gives better accuracy.

In [6] and [7], a mesh-free model was proposed in which the skin effect was modeled by approximating the flux-density distribution in the lamination depth by a set of orthogonal basis functions. The coefficients of the basis functions were solved from a single system of nonlinear equations. In [8], the basis functions were chosen to be cosine terms which made it possible to utilize Fourier analysis in the calculation and to use analytical integration formulas when forming the FE equations. If the Fourier coefficients of the flux-density are expressed using corresponding vector potential components, the mesh-free approach yields a single system of equations in which the eddy currents are globally coupled to the 2-D field solution. The number of unknowns in this system is typically smaller than is the case with the method presented earlier in [5].

In this paper, hysteretic material properties and excess losses are introduced to the mesh-free eddy-current model allowing full inclusion of the iron losses into the 2-D calculation. An inverted vector Preisach model is applied and both the hysteresis and excess losses are considered locally in the lamination depth. The three loss components and the global 2-D field distribution are strongly coupled and all the phenomena are modeled by solving a single system of equations thus achieving excellent convergence with the Newton-Raphson method.

The parameters of the proposed model are identified from a set of measurements performed for electrical steel sheet samples. Finally, the model is applied to predict core losses of a 37-kW induction motor. Results from the model correspond well with measured core losses.

2. The Lamination Model

2.1. Eddy Currents

The eddy currents in a ferromagnetic lamination oppose the penetration of the flux density into the sheet. If the edge effects are neglected and the eddy currents are assumed to flow parallel to the lamination surface, the magnetodynamic field in the

lamination is described by the diffusion equation

$$\frac{\partial^2 \boldsymbol{h}(z,t)}{\partial z^2} = \sigma \frac{\partial \boldsymbol{b}(z,t)}{\partial t}, \tag{1}$$

where z is the direction in the lamination depth, and the magnetic flux density $\boldsymbol{b} = b_x \boldsymbol{u}_x + b_y \boldsymbol{u}_y$ and field strength $\boldsymbol{h} = h_x \boldsymbol{u}_x + h_y \boldsymbol{u}_y$ are assumed to be parallel to the lamination and perpendicular to the z-axis. Depending on what kind of a material model (i.e. the constitutive relation $\boldsymbol{h} = \boldsymbol{h}(\boldsymbol{b})$) is used, vectors $\boldsymbol{h}(z,t)$ and $\boldsymbol{b}(z,t)$ may or may not be parallel to each other locally inside the lamination [9]. The electrical conductivity σ is assumed to be constant for a specific lamination material.

In [6]–[8], a mesh-free lamination model was developed to include the eddy-current effects into the FE implementation. The model is based on approximating the flux-density distribution in the lamination depth $z \in [-d/2, d/2]$ as a truncated Fourier cosine series with N_b terms:

$$\boldsymbol{b}(z,t) = \sum_{n=0}^{N_b-1} \boldsymbol{b}_n(t)\,\alpha_n(z) \text{ with } \alpha_n(z) = \cos\left(2n\pi \frac{z}{d}\right). \tag{2}$$

In a similar way, the field strength is approximated as

$$\boldsymbol{h}_{\text{appr}}(z,t) = \boldsymbol{h}_s(t) - \sigma d^2 \sum_{n=0}^{N_b-1} \frac{\partial \boldsymbol{b}_n(t)}{\partial t} \beta_n(z), \tag{3}$$

where $\boldsymbol{h}_s(t)$ is the field strength on the lamination surface and functions $\beta_n(z)$ are defined so that $\beta_n(\pm d/2) = 0$ and

$$\alpha_n(z) = -d^2 \frac{\partial^2 \beta_n(z)}{\partial z^2}. \tag{4}$$

With these approximations, $\boldsymbol{b}(z,t)$ and $\boldsymbol{h}_{\text{appr}}(z,t)$ satisfy (1) identically. Since the number of basis functions is finite, the error $\boldsymbol{\varepsilon}(z,t) = \boldsymbol{h}_{\text{appr}}(z,t) - \boldsymbol{h}(z,t)$ between the approximation $\boldsymbol{h}_{\text{appr}}(z,t)$ and the actual field strength $\boldsymbol{h}(z,t) = \boldsymbol{h}(\boldsymbol{b}(z,t))$ obtained from the constitutive material law cannot be identically zero, and is thus set to weakly satisfy

$$\frac{1}{d} \int_{-d/2}^{d/2} \boldsymbol{\varepsilon}(z,t)\,\alpha_n(z)\,dz = 0 \text{ for } n = 0, \ldots, N_b - 1, \tag{5}$$

from which the following equation system is obtained for the surface field strength:

$$\begin{bmatrix} \boldsymbol{h}_s(t) \\ 0 \\ \vdots \end{bmatrix} = \frac{1}{d} \int_{-d/2}^{d/2} \boldsymbol{h}(z,t) \begin{bmatrix} \alpha_0(z) \\ \alpha_1(z) \\ \vdots \end{bmatrix} dz + \sigma d^2 \boldsymbol{C} \frac{\partial}{\partial t} \begin{bmatrix} \boldsymbol{b}_0(t) \\ \boldsymbol{b}_1(t) \\ \vdots \end{bmatrix}. \tag{6}$$

The elements of the constant matrix $\boldsymbol{C}$ are obtained by integration over the lamination thickness as

$$C_{mn} = \frac{1}{d} \int_{-d/2}^{d/2} \alpha_m(z)\beta_n(z)\,dz\,, \tag{7}$$

where the indexing starts from zero to correspond with the indices of the basis functions.

Cosines were chosen as the basis functions because they form an orthogonal basis by definition, which leads to the useful fact that the spatial average flux density in the lamination is equal to the first term $\boldsymbol{b}_0$. In addition, the cosine functions need no further derivation in case a higher order approximation is desired. The availability of efficient fast Fourier transform routines also makes it possible to evaluate the required integrals analytically when the cosine series expansion is used, as will be seen later. However, if seen reasonable, the basis functions can also be chosen otherwise. For example, polynomial and hyperbolic basis functions were suggested in [6] and [7]. Hyperbolic functions could be a natural choice in a magnetically linear case, in which the flux-density distribution actually has a hyperbolic shape. However, in the highly nonlinear case dealt with in this paper, the advantage is not as trivial.

It should be noted that if only the average term $\boldsymbol{b}_0(t)$ is considered, and the higher-order terms are neglected, (6) reduces to

$$\boldsymbol{h}_{\mathrm{s}}(t) = \frac{1}{d} \int_{-d/2}^{d/2} \boldsymbol{h}(z,t)\,dz + \frac{\sigma d^2}{12} \frac{\partial \boldsymbol{b}_0(t)}{\partial t}\,, \tag{8}$$

which is the classical low-frequency approximation for the eddy-currents presented e.g. in [1].

2.2. Hysteresis

In ferromagnetic materials, the relation between the flux density $\boldsymbol{b}(z)$ and the field strength $\boldsymbol{h}(z)$ is hysteretic. To include the effect of hysteresis into the eddy-current model, the field strength $\boldsymbol{h}(z)$ in system (6) must be obtained from a suitable hysteresis model as a function of the flux density $\boldsymbol{b}(z)$. In this work, an isotropic inverted vector Preisach model presented in [10] and [11] was used.

The inverted Preisach model is based on modeling the first-order reversal curves by a pre-calculated inverted Everett function F. The field strength is obtained from F as

$$h_{\mathrm{hy}} = -F\left(-b_0^+, b_0^-\right) + 2\sum_{k=1}^{n_{\mathrm{rev}}} \left[F\left(b_k^+, b_{k-1}^-\right) - F\left(b_k^+, b_k^-\right) \right], \tag{9}$$

where $F(b_k^+,b_k^-)$ corresponds to reversal point k of the flux density and $F(-b_0^+,b_0^-)$ is the inverted Everett weight of the demagnetization state. The subscripts + and – refer to the increasing and decreasing values of the input flux density b, respectively [10].

In the vector model, the components of the field-strength vector $\boldsymbol{h}_{\mathrm{hy}}$ are obtained by projecting the flux density $\boldsymbol{b}$ into N_ϕ equally distributed directions $\boldsymbol{u}_{\phi,i}$, $i = 1,\ldots, N_\phi$, applying the scalar model to these projections $b_{\phi,i} = \boldsymbol{b} \cdot \boldsymbol{u}_{\phi,i}$ and summing the

outputs to form the field-strength vector [11]:

$$\boldsymbol{h}_{\mathrm{hy}} = \sum_{i=1}^{N_\phi} h_{\mathrm{hy}}\left(b_{\phi,i}\right)\boldsymbol{u}_{\phi,i} \ . \tag{10}$$

The Preisach model is able to accurately predict the minor hysteresis loops, making it an attractive choice for loss prediction in electrical machines where distorted flux-density waveforms occur. The inverted Everett function F must be obtained by measurements and supplied to the model as parameter data.

2.3. Excess Field

The term "excess loss" is often used to describe the difference between the actually measured eddy-current loss and the loss predicted by the classical eddy-current loss model (8). This difference has traditionally been explained by microscopic eddy currents induced by domain wall movement locally in the lamination [12]. As presented in [1], the excess losses can be accounted for in the field calculation by locally considering an excess field-strength term

$$\boldsymbol{h}_{\mathrm{ex}}\left(z,t\right) = \sqrt{\sigma G V_0 S}\left|\frac{\partial \boldsymbol{b}\left(z,t\right)}{\partial t}\right|^{-0.5}\frac{\partial \boldsymbol{b}\left(z,t\right)}{\partial t} \tag{11}$$

in addition to the term obtained from the hysteresis model. Here S is the cross-sectional area of the lamination, and V_0 and G are related to the magnetic properties of the lamination material according to [12].

An alternative explanation for the excess loss was presented in [13]. Since the classical eddy-current loss in [12] was assumed to correspond to a uniform flux density in the lamination and neglecting the skin effect, accurate modeling of the flux-density distribution according to (1) can at least partly compensate the difference between the measured and calculated eddy-current loss. The skin effect causes an increase in the classical eddy-current loss in nonlinear materials and the excess loss is reduced by definition. Thus the contribution of the excess field to the total field may actually be smaller than predicted by [12] if the skin effect is modeled accurately, as is the case in this study.

2.4. Losses

The local eddy-current loss density (in W/m^3) is obtained from the electric field strength $\boldsymbol{e} = e_{\mathrm{x}}\boldsymbol{u}_{\mathrm{x}} + e_{\mathrm{y}}\boldsymbol{u}_{\mathrm{y}}$ as

$$p_{\mathrm{cl}}\left(z,t\right) = \sigma\left|\boldsymbol{e}\left(z,t\right)\right|^2 = \sigma\left[\boldsymbol{e}\left(z,t\right)\cdot\boldsymbol{e}\left(z,t\right)\right]. \tag{12}$$

According to Faraday's induction law, the curl of the electric field strength is equal to the negative time derivative of the magnetic flux density:

$$\nabla \times \boldsymbol{e}(z,t) = -\frac{\partial e_{\mathrm{y}}(z,t)}{\partial z}\boldsymbol{u}_{\mathrm{x}} + \frac{\partial e_{\mathrm{x}}(z,t)}{\partial z}\boldsymbol{u}_{\mathrm{y}} = -\frac{\partial \boldsymbol{b}(z,t)}{\partial t}. \tag{13}$$

The components of $\boldsymbol{e}$ can be obtained from (13) by integration. Substituting them to (12) gives the eddy-current loss density in the lamination depth as

$$\begin{aligned} p_{\mathrm{cl}}(z,t) &= \sigma\left(\int \frac{\partial \boldsymbol{b}(z,t)}{\partial t}dz\right)\cdot\left(\int \frac{\partial \boldsymbol{b}(z,t)}{\partial t}dz\right) \\ &= \sigma\sum_{m=0}^{N_{\mathrm{b}}-1}\sum_{n=0}^{N_{\mathrm{b}}-1}\frac{\partial \boldsymbol{b}_m(t)}{\partial t}\cdot\frac{\partial \boldsymbol{b}_n(t)}{\partial t}\int \alpha_m(z)dz\int \alpha_n(z)dz. \end{aligned} \tag{14}$$

The average power loss density dissipated during one full cycle T of the flux density is

$$p_{\mathrm{cl,av}}(z) = \frac{1}{T}\int_T p_{\mathrm{cl}}(z,t)dt. \tag{15}$$

When the magnitude of magnetic field strength is increased, energy needs to be supplied into the magnetic field. In anhysteretic media, the same amount of energy is released when the field strength is reduced back to its original value. In hysteretic materials, however, a certain amount of the supplied energy is dissipated as heat in the Barkhausen jumps when the magnetic domains are rearranging [14]. Although it is difficult to determine this instantaneous hysteresis loss dissipation, the average value of the loss in a steady state is equal to the average of the energy supplied into the material during one full cycle of the flux density. The other parts of the energy only contribute to the reactive power which alternates between the power source and the material but has a zero mean value. Thus the hysteresis loss is here defined as the average value over one cycle, and instantaneous hysteresis loss is not considered:

$$p_{\mathrm{hy,av}}(z) = \frac{1}{T}\int_T \boldsymbol{h}_{\mathrm{hy}}(z,t)\cdot\frac{\partial \boldsymbol{b}(z,t)}{\partial t}dt. \tag{16}$$

Correspondingly, the average excess loss is calculated as

$$p_{\mathrm{ex,av}}(z) = \frac{1}{T}\int_T \boldsymbol{h}_{\mathrm{ex}}(z,t)\cdot\frac{\partial \boldsymbol{b}(z,t)}{\partial t}dt = \sqrt{\sigma G V_0 S}\,\frac{1}{T}\int_T \left|\frac{\partial \boldsymbol{b}(z,t)}{\partial t}\right|^{1.5} dt. \tag{17}$$

2.5. Implementation

Equation (6) is solved with a suitable time-stepping method. Here the backward Euler approximation is applied for the time discretization:

$$\begin{bmatrix} \boldsymbol{h}_\mathrm{s} \\ 0 \\ \vdots \end{bmatrix} = \frac{1}{d}\int_{-d/2}^{d/2} \boldsymbol{h}(z) \begin{bmatrix} \alpha_0(z) \\ \alpha_1(z) \\ \vdots \end{bmatrix} dz + \frac{\sigma d^2}{\Delta t} \boldsymbol{C} \begin{bmatrix} \boldsymbol{b}_0 \\ \boldsymbol{b}_1 \\ \vdots \end{bmatrix} - \boldsymbol{f} \,, \tag{18}$$

where Δt is the time-step length and $\boldsymbol{f}$ contains values from the previous time step. Equation (11) becomes

$$\boldsymbol{h}_\mathrm{ex}(z) = \sqrt{\sigma G V_0 S} \left| \frac{\boldsymbol{b}(z) - \boldsymbol{b}_\mathrm{p}(z)}{\Delta t} \right|^{-0.5} \left(\frac{\boldsymbol{b}(z) - \boldsymbol{b}_\mathrm{p}(z)}{\Delta t} \right), \tag{19}$$

where $\boldsymbol{b}_\mathrm{p}(z)$ is the value of the flux density on the previous step.

Due to the nonlinear and hysteretic material characteristics system (18) is nonlinear and thus an iterative approach is required to obtain the solution. In [15], the fixed-point (FP) technique was adopted to handle the nonlinearity. In hysteretic materials, both the reluctivity and its derivative with respect to the flux density may have any value between positive and negative infinity. Since the FP method does not require accurate calculation of the derivative and uses a fixed finite value for the reluctivity, it was found reasonable when dealing with hysteretic materials. However, the convergence rate of the FP technique is usually much slower than, for instance, that of the Newton-Raphson (NR) method which utilizes the derivatives to achieve quadratic convergence.

In this paper, the NR method is applied by utilizing the differential reluctivity which is always well defined also for hysteretic materials [16], [17]. If the derivative of the m^th equation in (18) is taken with respect to the n^th flux-density component, a submatrix of the total Jacobian needed in the solution is obtained:

$$\boldsymbol{J}_{m,n} = \frac{1}{d}\int_{-d/2}^{d/2} \frac{\partial \boldsymbol{h}}{\partial \boldsymbol{b}} \alpha_m \alpha_n dz + \frac{\sigma d^2}{\Delta t} C_{mn} \boldsymbol{I} \,, \tag{20}$$

where $\boldsymbol{I}$ is the 2×2 identity matrix. The differential reluctivity tensor $\partial \boldsymbol{h}/\partial \boldsymbol{b}$ is positive definite which should guarantee good convergence. Similarly to the field strength, the differential reluctivity consists of two parts corresponding to the hysteresis and excess losses:

$$\frac{\partial \boldsymbol{h}}{\partial \boldsymbol{b}} = \begin{bmatrix} \dfrac{\partial h_\mathrm{x}}{\partial b_\mathrm{x}} & \dfrac{\partial h_\mathrm{x}}{\partial b_\mathrm{y}} \\ \dfrac{\partial h_\mathrm{y}}{\partial b_\mathrm{x}} & \dfrac{\partial h_\mathrm{y}}{\partial b_\mathrm{y}} \end{bmatrix} = \frac{\partial \boldsymbol{h}_\mathrm{hy}}{\partial \boldsymbol{b}} + \frac{\partial \boldsymbol{h}_\mathrm{ex}}{\partial \boldsymbol{b}} \,. \tag{21}$$

The hysteretic part can be calculated based on (10) as

$$\frac{\partial \boldsymbol{h}_\mathrm{hy}}{\partial \boldsymbol{b}} = \sum_{i=1}^{N_\phi} \frac{\partial h_\mathrm{hy}}{\partial b_{\phi,i}} \frac{\partial b_{\phi,i}}{\partial \boldsymbol{b}} \boldsymbol{u}_{\phi,i} = \sum_{i=1}^{N_\phi} \frac{\partial h_\mathrm{hy}}{\partial b_{\phi,i}} \begin{bmatrix} \cos\phi_i \\ \sin\phi_i \end{bmatrix} \begin{bmatrix} \cos\phi_i \\ \sin\phi_i \end{bmatrix}^\mathrm{T} \,, \tag{22}$$

where $\partial h_\mathrm{hy}/\partial b_{\phi,i}$ is the differential reluctivity obtained from the scalar model in direction $\boldsymbol{u}_{\phi,i}$. The excess-loss part is obtained by

differentiating (19):

$$\frac{\partial \boldsymbol{h}_{\mathrm{ex}}}{\partial \boldsymbol{b}} = \sqrt{\frac{\sigma G V_0 S}{\Delta t}} \left| \boldsymbol{b} - \boldsymbol{b}_{\mathrm{p}} \right|^{-0.5} \left[\boldsymbol{I} - 0.5 \frac{\left(\boldsymbol{b} - \boldsymbol{b}_{\mathrm{p}} \right) \left(\boldsymbol{b} - \boldsymbol{b}_{\mathrm{p}} \right)^{\mathrm{T}}}{\left| \boldsymbol{b} - \boldsymbol{b}_{\mathrm{p}} \right|^2} \right]. \tag{23}$$

In a relatively straightforward manner applying (22) and (23), it can be shown that $\boldsymbol{x}^{\mathrm{T}}(\partial \boldsymbol{h}/\partial \boldsymbol{b})\boldsymbol{x} > 0$ for all nonzero vectors $\boldsymbol{x}$ which means that the differential reluctivity tensor is positive definite, as stated earlier. For brevity, the proof is ignored in this paper.

Since cosine functions were used as the basis functions, the integrations in (18) and (20) can be performed analytically, if a fast cosine transform (FCT) is first performed for the field strength and for the differential reluctivity. The flux density is sampled in the lamination depth and an FCT algorithm is applied to obtain the field strength as

$$\boldsymbol{h}(z) \approx \sum_{n=0}^{N_{\mathrm{h}}-1} \boldsymbol{h}_n \alpha_n(z). \tag{24}$$

After this, the integration in (18) becomes

$$\int_{-d/2}^{d/2} \boldsymbol{h}(z) \begin{bmatrix} \alpha_0(z) \\ \alpha_1(z) \\ \vdots \end{bmatrix} dz \approx \sum_{n=0}^{N_{\mathrm{h}}-1} \boldsymbol{h}_n \int_{-d/2}^{d/2} \alpha_n \begin{bmatrix} \alpha_0(z) \\ \alpha_1(z) \\ \vdots \end{bmatrix} dz \tag{25}$$

in which the integrand is now only a product of two cosine terms and can be integrated analytically at the preprocessing stage. In fact, based on the definition of the cosine series, the integration on line m in (25) always results in term $\boldsymbol{h}_m$. Due to the orthogonality property of the basis functions, it is enough to select $N_{\mathrm{h}} = N_{\mathrm{b}}$, since for the terms $n \geq N_{\mathrm{b}}$ the integral (25) is zero.

Since the relationship between the flux density and field strength is nonlinear, the field strength distribution may actually include more than N_{b} spatial harmonic components. To reduce aliasing of the higher order components to wave numbers 0, …, $N_{\mathrm{b}} - 1$, the number of sample points for the field strength has to be higher than $2N_{\mathrm{b}}$ which would be the theoretical minimum to obtain the FCT accurately in the linear case. A good convergence was obtained already with $4N_{\mathrm{b}}$ samples in the lamination depth. Since the flux density and field strength are symmetric with respect to the middle point of the lamination thickness, the number of samples can be further reduced to $2N_{\mathrm{b}} + 1$.

The integration in (20) can be treated similarly by performing the FCT for the differential reluctivity and integrating the resulting triple product of cosine terms analytically.

3. The 2-D Model

In 2-D finite element formulations for electrical machines, Ampere's circuital law

$$\nabla \times \boldsymbol{H} = \boldsymbol{J} \tag{26}$$

is solved in the machine cross section together with the required circuit equations [18], [19]. In the coils and solid core regions, the current density $\boldsymbol{J}$ is assumed to have only axial component and the magnetic field $\boldsymbol{H}$ does not depend on the axial position z. In conventional 2-D FE formulations with lamination eddy currents neglected, the previous assumptions (with $\boldsymbol{J} = 0$) are also valid in the laminated core regions. However, when the presented lamination loss model is considered, the eddy currents and skin effect cause the magnetic field to be non-uniform in the lamination which must be taken into account also in the 2-D formulation. To handle this, the del operator is divided in two parts:

$$\nabla = \nabla_{\mathrm{xy}} + \nabla_{\mathrm{z}} \text{ with } \nabla_{\mathrm{xy}} = \boldsymbol{u}_{\mathrm{x}} \frac{\partial}{\partial x} + \boldsymbol{u}_{\mathrm{y}} \frac{\partial}{\partial y}, \quad \nabla_{\mathrm{z}} = \boldsymbol{u}_{\mathrm{z}} \frac{\partial}{\partial z}. \tag{27}$$

With these definitions, the equations to be solved in the laminated core regions of the 2-D cross-section become

$$\nabla_{\mathrm{xy}} \times \boldsymbol{H} = 0 \tag{28}$$

$$\nabla_{\mathrm{z}} \times \boldsymbol{H} = \boldsymbol{J}. \tag{29}$$

In all the other regions the equations are

$$\nabla_{\mathrm{xy}} \times \boldsymbol{H} = \boldsymbol{J} \tag{30}$$

$$\nabla_{\mathrm{z}} \times \boldsymbol{H} = 0, \tag{31}$$

where $\boldsymbol{J} = 0$ in air and non-conducting regions with no source-current terms. Obviously, Ampere's law (26) is satisfied in the whole geometry.

In the laminated core regions, the current density $\boldsymbol{J}$ consists fully of the lamination eddy currents and depends on the time variation of the flux density according to

$$\nabla_{\mathrm{z}} \times \boldsymbol{J}\left(x, y, z, t\right) = -\sigma \frac{\partial \boldsymbol{B}\left(x, y, z, t\right)}{\partial t}. \tag{32}$$

The solution for (29) and (32) together was already obtained in (6). As shown e.g. in [20], the relation between the surface field strength $\boldsymbol{H}_{\mathrm{s}}$ and the average flux density $\boldsymbol{B}_0$ over the lamination thickness includes all the effects of the iron losses inside the lamination. Thus these effects can be accounted for in the 2-D FE model simply by applying Ampere's law to the surface term $\boldsymbol{H}_{\mathrm{s}} = \boldsymbol{H}_{\mathrm{s}}(x,y,t)$. This yields the time-discretized equation system

$$\frac{1}{d}\nabla_{\mathrm{xy}}\times\int_{-d/2}^{d/2}\boldsymbol{H}\begin{bmatrix}\alpha_0\\ \alpha_1\\ \vdots\end{bmatrix}dz+\frac{\sigma d^2}{\Delta t}\boldsymbol{C}\nabla_{\mathrm{xy}}\times\begin{bmatrix}\boldsymbol{B}_0\\ \boldsymbol{B}_1\\ \vdots\end{bmatrix}-\nabla_{\mathrm{xy}}\times\boldsymbol{F}=0\,. \tag{33}$$

Capital letters are used here to emphasize the x and y dependency of the 2-D quantities, and the curl operator is applied to each component $\boldsymbol{B}_m$ and $\boldsymbol{H}\alpha_m$ separately. In principle, the curl only needs to be applied to the first equation, since that one gives the surface field strength. However, to keep the total system matrix symmetric, the curl is applied also to the rest of the equations.

A numerical solution of (33) requires spatial discretization which is performed by discretizing the cross-section into finite elements and applying the Galerkin weighted residual method [19]. Discretizing the m^{th} equation of the system leads to the subsystem

$$\int_{\Omega}\boldsymbol{D}^{\mathrm{T}}\left(\frac{1}{d}\int_{-d/2}^{d/2}\boldsymbol{H}\alpha_m dz+\frac{\sigma d^2}{\Delta t}\sum_{n=0}^{N_{\mathrm{b}}-1}C_{mn}\boldsymbol{B}_n-\boldsymbol{F}_m\right)d\Omega=0\,, \tag{34}$$

where

$$\boldsymbol{D}=\begin{bmatrix}\dfrac{\partial N_1}{\partial y} & \dfrac{\partial N_2}{\partial y} & \cdots & \dfrac{\partial N_N}{\partial y}\\ -\dfrac{\partial N_1}{\partial x} & -\dfrac{\partial N_2}{\partial x} & \cdots & -\dfrac{\partial N_N}{\partial x}\end{bmatrix} \tag{35}$$

is the discrete curl operator $\nabla_{\mathrm{xy}}\times$ expressed using the N spatial shape functions $N_1(x,y)$, $N_2(x,y)$, …, $N_N(x,y)$ and Ω denotes the laminated regions in the solution geometry. The discretized equation system to be solved in the laminated core regions consists of $N_{\mathrm{b}}N$ equations in total. This system can be solved in terms of the nodal values of the axial magnetic vector potential components $\boldsymbol{a}_n=(a_{n,1},\ldots,a_{n,N})$, with $n=0,\ldots,N_{\mathrm{b}}-1$ corresponding to the flux-density components:

$$\boldsymbol{B}_n(x,y,t)=\nabla_{\mathrm{xy}}\times\boldsymbol{A}_n(x,y,t)=\nabla_{\mathrm{xy}}\times\sum_{j=1}^{N}a_{n,j}(t)N_j(x,y)\boldsymbol{u}_{\mathrm{z}}. \tag{36}$$

The total system Jacobian matrix needed in the NR iteration consists of $N_{\mathrm{b}}N_{\mathrm{b}}$ submatrices with sizes of $N\times N$ each. The 2-D submatrix corresponding to (20) is $\boldsymbol{D}^{\mathrm{T}}\boldsymbol{J}_{m,n}\boldsymbol{D}$.

To ensure a unique solution, suitable boundary conditions are needed for the vector potentials. All the vector potential components $\boldsymbol{A}_n$, $n=0,\ldots,N_{\mathrm{b}}-1$ are set to zero on the outer boundary of the stator to ensure that the flux stays inside the machine. In addition, the components $n=1,\ldots,N_{\mathrm{b}}-1$ are set to zero on the boundary between the laminated rotor and the solid steel shaft. This additional condition is needed since the higher-order vector-potential components are not solved in the air gap and thus the stator-side boundary condition is not enough to ensure a unique solution on the rotor side.

The possibility of applying vector potential components provides global coupling of the eddy-current effects to the field

solution. In [5], local coupling was used since the eddy-current effects were merely included in the dynamic B-H relationship, and were thus considered as material properties. Since the number of nodes is typically smaller than the required number of 2-D integration points in the whole geometry, the globally coupled approach with the vector potentials easily results in fewer unknowns than is the case with the locally coupled one.

4. Application and Results

4.1. Parameter Identification

If the lamination thickness and conductivity are known, only the inverted Everett function in the Preisach model and the excess loss coefficient need to be identified. The presented lamination model was identified by best fitting simulation results to B-H loop measurements performed for 0.5 mm electrical steel sheets used as the core material in an induction motor. The measurements were done with a 2-D vertical rotational single-sheet tester [21], [22] allowing independent supply of the x and y components of the average flux density in the lamination. Several loops were measured with different average flux-density amplitudes and supply frequencies. Since the conductivity of the sheet material was not known accurately, it was set as one extra parameter in the fitting procedure which was implemented in the least squares sense.

The measured average flux-density waveform was supplied to the model, and the fitting was performed by comparing the surface field strength obtained from the model to that obtained from the measurements. The Everett function was first identified from a low-frequency measurement. Next, the conductivity and the excess-loss coefficient were identified by best fitting the simulation results at 20, 100 and 500 Hz supply and average flux-density amplitudes from 0.6 to 1.4 T. The obtained values were $\sigma = 3.12$ MS/m and $(\sigma G V_0 S)^{1/2} = 9.39\times10^{-5}$ (W/kg)(s/T)$^{3/2}$. The best-fitted B-H loops with alternating flux density are shown in Figure 1. Figure 2 shows 2-D loci of the surface field strength with 500 Hz rotational flux-density supplies. The supplied flux density is not exactly circular but varies a bit in amplitude, which causes the simulated field strength to appear slightly anisotropic despite the isotropic nature of the model. Based on these results, the model is able to predict the physical behavior of the magnetic field in the sheet reasonably well.

4.2. Core Losses of an Induction Motor

With the identified iron-loss model, a 400-V, 37-kW cage-induction motor was simulated, the core losses of which have been measured under no-load conditions at different voltages. The ratings and some dimensions of the machine are listed in Table 1. The method of measuring the no-load losses was described in [23] and [24]. The measurements were performed by rotating the induction machine by a speed-controlled slip-ring motor and averaging the powers taken by the machine from the network at small positive and negative slips. In such a way, the sudden change in the input power at zero slip caused by the rotor remanence

flux can be eliminated, and the terminal input power only comprises the stator resistive loss and the core loss, which here means the sum of iron losses and the rotor bar resistive losses. The mechanical losses are supplied by the slip-ring motor. The stator resistance at the operating point temperature was determined by stopping and de-energizing the machine, measuring the resistance as a function of time during the first couple of minutes when the machine was cooling down, and extrapolating to the switch-off instant assuming exponential form of the cooling curve. After the resistance was known, the core loss was obtained by subtracting the stator resistive loss from the input power. As discussed in [23], the uncertainty in the measured core loss increases with the voltage, since the proportion of the stator resistive loss on the total loss becomes higher. The error is less than 3 % at and below the rated voltage 400 V, but rises close to 8.5 % when the voltage is increased to 500 V.

After some numerical experiments, $N_\mathrm{b} = 2$ cosine terms were chosen to be used for the flux density to model the skin effect in the calculation. Adding more terms didn't significantly change the results in this case, but only slowed down the computation. In the simulations, the no-load operation was forced by setting the rotor to rotate at zero slip while supplying the stator winding from a voltage source. An initial state for the time-stepping simulation was obtained with a time-harmonic model. 800 time steps per one supply period of 0.02 s were enough to obtain a good convergence in the Newton-Raphson iteration and to model the rotor harmonic frequencies accurately up to the kilohertz range, while keeping the computation time reasonable. The machine was simulated for two periods to reduce the transients in the time stepping. Since the slip was set to zero, no low-frequency flux existed in the rotor, and the hysteresis loops in all the 2-D elements made at least one full closed cycle during the latter supply period.

For comparison, the motor was also modeled without the lamination model using single-valued (SV) material characteristics. In this case, the iron losses were obtained based on the statistical loss theory [12] as superposition of the losses obtained for each time-harmonic component of the average flux density separately:

$$p_\mathrm{Fe} = \sum_{n=1}^{100} \left(c_\mathrm{hy} \omega_n + c_\mathrm{cl} \omega_n^2 \right) \left| \boldsymbol{B}_{0,n} \right|^2 , \tag{37}$$

where c_hy and c_cl are the loss coefficients given by the sheet manufacturer and ω_n is the frequency of the average flux-density harmonic $\boldsymbol{B}_{0,n}$.

To illustrate the skin effect, the distributions of the two Fourier components for the flux density at 400 V are plotted in Figure 3. The second component $\boldsymbol{B}_1$ seems to be at maximum on those regions where the average flux density $\boldsymbol{B}_0$ has its minimum value. On these regions $\boldsymbol{B}_0$ is changing rapidly as the magnetic field is rotating, which increases the significance of the skin effect and thus the value of $\boldsymbol{B}_1$. The high values of the average flux density show that the iron is saturated already at the rated voltage.

The average flux density and surface field strength near the root of the stator tooth and in the tip of the rotor tooth (points A and B in Figure 3) are plotted in Figure 4. In these points the flux density has a significant rotational component which implies

that the use of a vector hysteresis model is essential for accurate analysis of such complex electromechanical devices. From the closed B-H loops, it can be seen that the system is magnetically in a steady state.

The no-load currents and core losses are compared in Figure 5. The current is predicted accurately both by the proposed model and the SV model which implies that the material properties are correctly modeled up to saturation. However, the losses obtained from the proposed model correspond significantly better with the measured ones than those obtained from the SV model. This shows the importance of accurate modeling of the magnetic field in the core laminations. Still, the greatest error occurs at the highest studied voltage when the motor is most saturated.

Figure 6 segregates the core loss into hysteresis, eddy-current, excess and rotor bar losses. Hysteresis loss accounts for over half of the core loss until high saturation is reached at 500 V. The eddy-current loss increases somewhat quadratically and the excess loss nearly linearly when the terminal voltage is increased. The rotor bar resistive losses become significant only above the rated voltage.

Distributions of the iron-loss components near the air gap at 400 V are plotted in Figure 7. The hysteresis loss is the dominant loss component both on the stator and rotor sides. The eddy currents are induced by the air-gap flux density harmonics and forced to the surface of the rotor by the rotor bars. The excess loss is at the maximum on the iron bridges above the rotor slots. However, its proportion on the total loss seems almost negligible.

4.3. Computational Efficiency Considerations

The 2-D mesh consisted of 1692 second order elements with 3777 nodes in total and three integration points per element. The core region, in which the lamination model was used, had 840 elements and 2176 nodes. The two cosine terms used in the lamination model and 13 voltage equations resulted in $2\times2176 + (3777 - 2176) + 13 = 5966$ equations for which the computation time was approximately 1 h 10 min in total and 2.6 s per time step in the 400 V simulation. The average number of NR iterations per time step was 6.55. None of the iterations diverged during the time stepping.

For comparison, if the directly coupled 2-D/1-D method in [5] was used for the same problem, even only with three divisions in the 1-D discretization, the formulation would result in $3777 + 2\times3\times3\times840 + 13 = 18910$ equations in total. This is over three times the amount obtained with the presented model. As already mentioned, global coupling using the vector potential and nodal values requires fewer unknowns than the local one, especially with second and higher-order elements when more integration points are needed in the 2-D elements.

5. Conclusion

A method for including hysteresis, eddy-current and excess losses into 2-D finite element analysis was presented. The method

allows full coupling of the three iron-loss phenomena and their inclusion to the magnetic field computation. A single nonlinear system of equations is solved by using the Newton-Raphson method and utilizing the differential reluctivity tensor. Excellent convergence is obtained despite the fact that the material properties are hysteretic and rate dependent due to the hysteresis and excess-loss effects.

Comparison with experimental measurements implies that the model is able to reasonably predict the iron losses also in complex electromechanical devices, such as the induction motor. Some error is obviously caused by the effect of punching and welding on the material properties in the actual machine, as well as inter-bar currents in the rotor core, which are not taken into account in the presented model. Despite the fact that the no-load currents seem to be modeled correctly, the iron-loss calculation is sensitive to the material parameters, especially to the shape of the static hysteresis loops. Inaccuracies in these may cause the overestimation of the losses at 500 V when significant saturation occurs, but also the higher measurement error in this point can partly explain the difference. Nevertheless, the model is able to give valuable information on the losses and their distribution for machine design and structural optimization purposes.

For best results, the flux-density range used in the fitting of the hysteresis loops should be extended as high as possible, preferably up to the point of maximum saturation above which the differential reluctivity corresponds to the reluctivity of vacuum. Another factor causing inaccuracy in the hysteresis-loss calculation is that when high saturation occurs, the instantaneous values of the magnetic energy density can be decades higher than its average over one full cycle. This makes the average hysteresis loss very sensitive to the instantaneous variations of the flux density.

The authors are aware that the results of the single-valued model used for comparison could possibly be significantly improved by optimizing the loss coefficients c_{hy} and c_{cl} by comparison to experimentally obtained loss data. However, the purpose here was to use the loss coefficients provided by the sheet manufacturer. The coefficients are usually determined for sinusoidally varying average flux density at a specific frequency, and the superposition of the losses calculated separately for each flux-density harmonic leads to erroneous results.

The efficiency analysis shows that the presented model provides a competitive alternative to other previously presented loss-prediction methods. Future applications will include analysis of losses in inverter-supplied electrical machines.

6. Acknowledgment

Paavo Rasilo thanks the Academy of Finland, the Fortum foundation, the Finnish Foundation for Economic and Technical Sciences (KAUTE), the Walter Ahlström foundation and the foundation of the Association of Electrical Engineers in Finland (Sähköinsinööriliiton Säätiö) for financial support.

7. References

[1] Righi, L.A., Sadowski, N., Carlson, R., Bastos, J.P.A., and Batistela, N.J.: 'A New Approach for Iron Losses Calculation in Voltage Fed Time Stepping Simulations', *IEEE Trans. Magn.*, 2001, 37, (5), pp. 3353-3356

[2] Dlala, E.: 'A Simplified Iron Loss Model for Laminated Magnetic Cores', *IEEE Trans. Magn.*, 2008, 44, (11), pp. 3169-3172

[3] Bottauscio, O., Chiampi, M., and Chiarabaglio, D.: 'Advanced Model of Laminated Magnetic Cores for Two-Dimensional Field Analysis', *IEEE Trans. Magn.*, 2000, 36, (3), pp. 561-573

[4] Dlala, E., Belahcen, A., and Arkkio, A.: 'Efficient magnetodynamic lamination model for two-dimensional field simulation of rotating electrical machines', *J. Magn. Magn. Mater.*, 2008, 320, (20), pp. 1006-1010

[5] Bottauscio, O., and Chiampi, M.: 'Analysis of Laminated Cores Through a Directly Coupled 2-D/1-D Electromagnetic Field Formulation', *IEEE Trans. Magn.*, 2002, 38, (5), pp. 2358-2360

[6] Gyselinck, J., Sabariego, R.V., and Dular P.: 'A Nonlinear Time-Domain Homogenization Technique for Laminated Iron Cores in Three-Dimensional Finite-Element Models', *IEEE Trans. Magn.*, 2006, 42, (4), pp. 763-766

[7] Dular, P.: 'A time-domain homogenization technique for lamination stacks in dual finite element formulations', *J. Comp. Appl. Math.*, 2008, 215, pp. 390-399

[8] Rasilo, P., and Arkkio, A.: 'A Mesh-Free Model of Eddy-Current Losses for 2D Analysis of Ferromagnetic Laminations', Compumag 2009, Florianópolis, Brazil, November 2009

[9] Del Vecchio, R.M.: 'The Calculation of Eddy Current Losses Associated with Rotating Magnetic Fields in Thin Laminations', *IEEE Trans. Magn.*, 1982, 18, (6), pp. 1707-1709

[10] Dlala, E., Saitz, J., and Arkkio, A.: 'Inverted and Forward Preisach Models for Numerical Analysis of Electromagnetic Field Problems', *IEEE Transactions on Magnetics*, 2006, 42, (8), pp. 1963-1973

[11] Dlala, E., Belahcen, A., and Arkkio, A.: 'Magnetodynamic vector hysteresis model of ferromagnetic steel laminations', *Physica B: Condensed Matter*, 2008, 403, (2-3), pp. 428-432

[12] Bertotti, G.: 'General Properties of Power Losses in Soft Ferromagnetic Materials', *IEEE Trans. Magn*., 1988, 24, (1), pp. 621-630

[13] Mayergoyz, I., and Serpico, C.: 'Nonlinear diffusion of electromagnetic fields and excess eddy current losses', *Journal of Applied Physics*, 1999, 85, (8), pp. 4910-4912

[14] Bertotti, G.: 'Hysteresis in magnetism for physicists, material scientists, and engineers', (Academic Press, 1998), p. 43

[15] Dlala, E., Belahcen, A., and Arkkio, A.: 'A Fast Fixed-Point Method for Solving Magnetic Field Problems in Media of Hysteresis', *IEEE Transactions on Magnetics*, 2008, 44, (6), pp. 1214-1217

[16] Dupré, L.R., Gyselinck, J.J., and Melkebeek, J.A.: 'Complimentary Finite Element Methods in 2D Magnetics Taking into Account a Vector Preisach Model', *IEEE Trans. Magn.*, 1998, 34, (5), pp. 3048-3051

[17] Gyselinck, J., Dular, P., Sadowski, N., Leite, J., and Bastos, J.P.A.: 'Incorporation of a Jiles-Atherton vector hysteresis model in 2D FE magnetic field computations, Application of the Newton-Raphson method', *COMPEL*, 2004, 23, (3), pp. 685-693

[18] Chari, M.V.K., and Silvester, P.: 'Analysis of Turboalternator Magnetic Fields by Finite Elements', *IEEE Trans. PAS*, 1971, 90, (2), pp. 454-464

[19] Arkkio, A.: 'Analysis of Induction Motors Based on the Numerical Solution of the Magnetic Field and Circuit Equations', Ph.D. Thesis, Helsinki University of Technology, Finland, December 1987, Available at http://lib.tkk.fi/Diss/198X/isbn951226076X/, pp. 14-16

[20] Atallah, K., and Howe, D.: 'Calculation of the Rotational Power Loss in Electrical Steel Laminations from Measured $\bar{H}$ and $\bar{B}$ ', *IEEE Trans. Magn.*, 1993, 29, (6), pp. 3547-3549

[21] Fonteyn, K., and Belahcen, A.: 'Numerical and Experimental Results from a Vertical Yoke System for Measuring Magnetic Properties of Fe-Si Steel Sheets', *Proceedings on ICEMS 2008, The 11th International Conference on Electrical Machines and Systems*, Wuhan, China, October 2008, pp. 434-438

[22] Fonteyn, K.: 'Energy-Based Magneto-Mechanical Model for Electrical Steel Sheets', Ph.D. Thesis, Aalto University School of Science and Technology, Finland, August 2010, Available at http://lib.tkk.fi/Diss/2010/isbn9789526032887/, pp. 67-70 and 128

[23] Saitz, J.: 'Magnetic Field Analysis of Electric Machines Taking Ferromagnetic Hysteresis into Account', Ph.D. Thesis, Helsinki University of Technology, Finland, November 2001, Available at http://lib.tkk.fi/Diss/2001/isbn9512256908/, p. 103

[24] Pippuri, J., and Arkkio, A.: 'Challenges in the segregation of losses in cage induction machines', *Proceedings of the 2008 International Conference on Electrical Machines*, Vilamoura, Portugal, September 2008

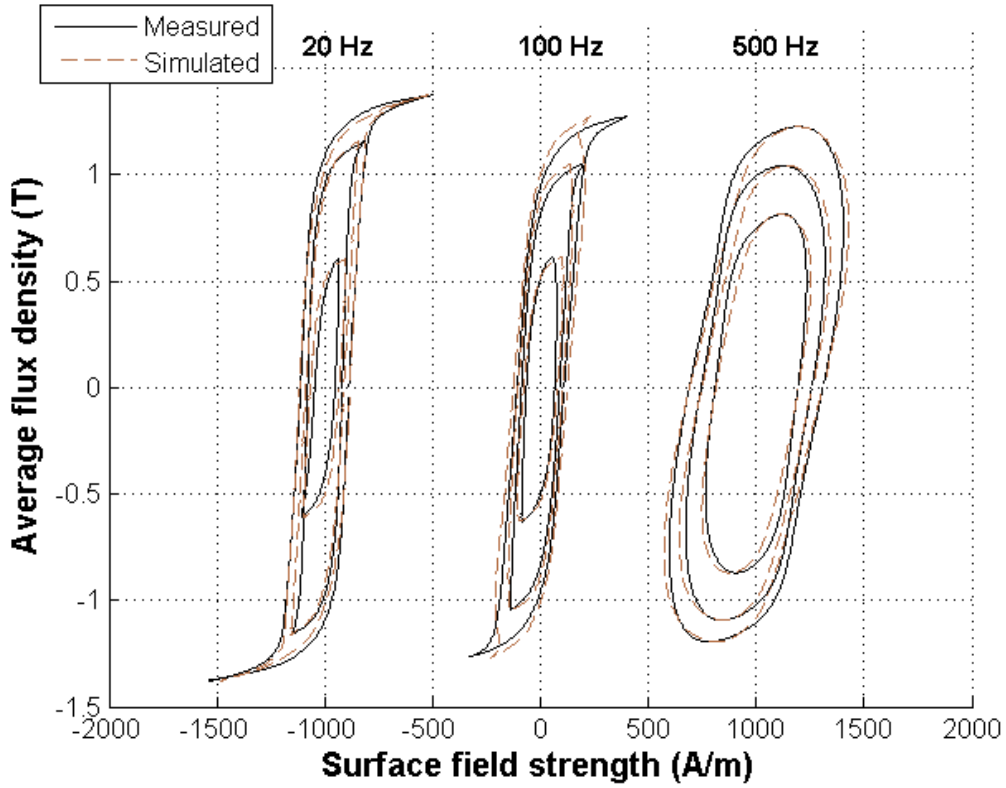

Figure 1 Best-fitted B-H loops with different frequencies and amplitudes. The 20 Hz and 500 Hz curves are shifted from the origin for clarity.

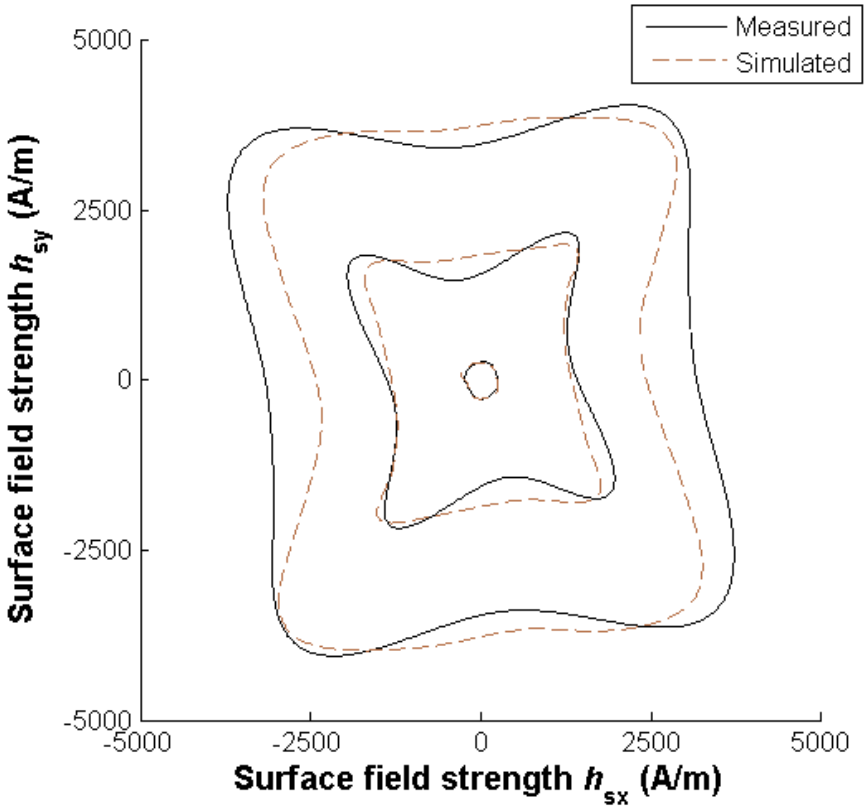

Figure 2 2-D loci of the surface field strength with 500 Hz rotational average flux density

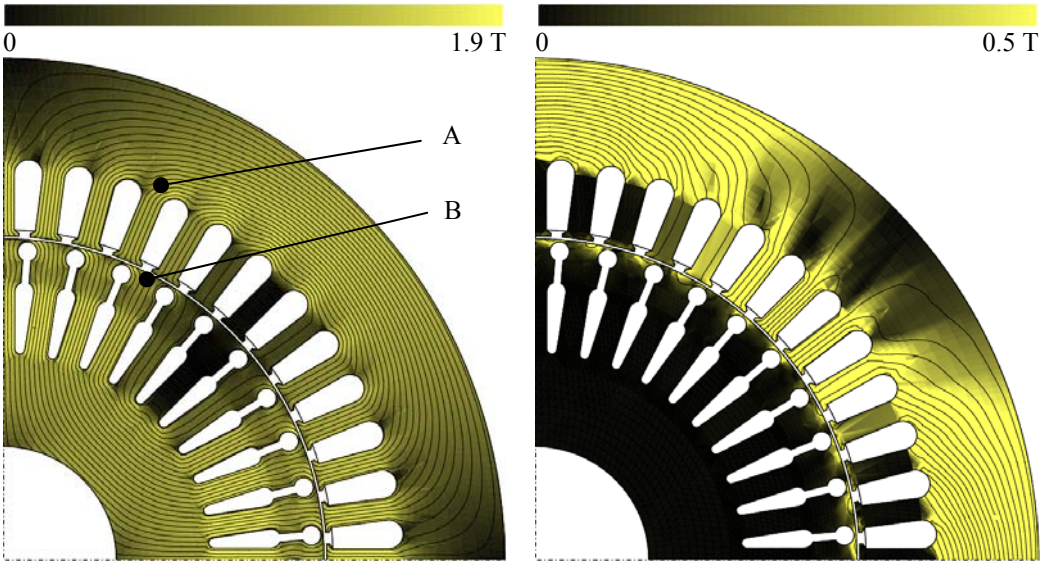

Figure 3 The two flux density components in the motor core at 400 V.
A and B denote the points in which the B-H loops of Figure 4 are calculated.

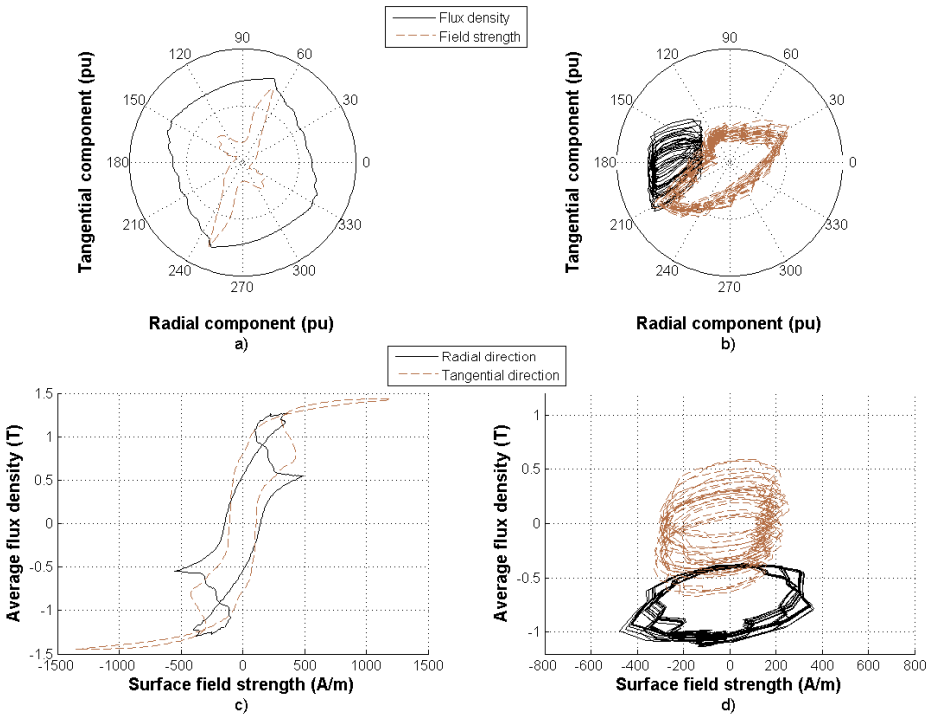

Figure 4 Normalized 2-D loci of the average flux density and surface field strength at a) stator point A and b) rotor point B.
B-H loops in both tangential and radial directions at c) stator point A and d) rotor point B.

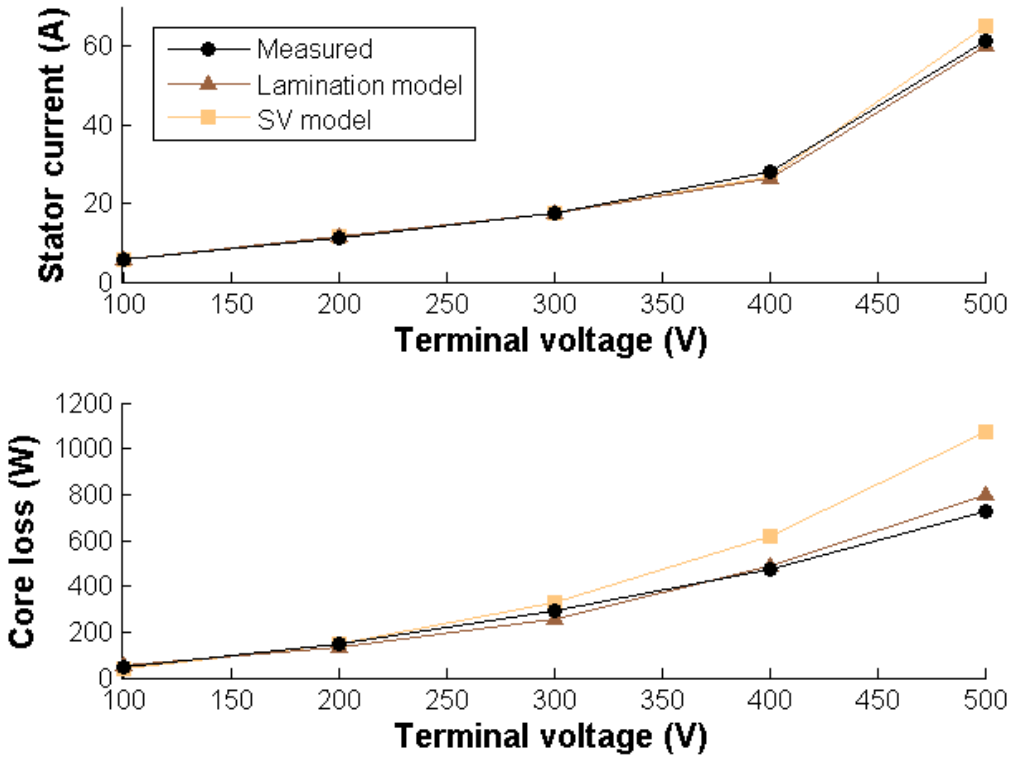

Figure 5 Stator current and core loss vs. terminal voltage in the induction motor in no-load operation

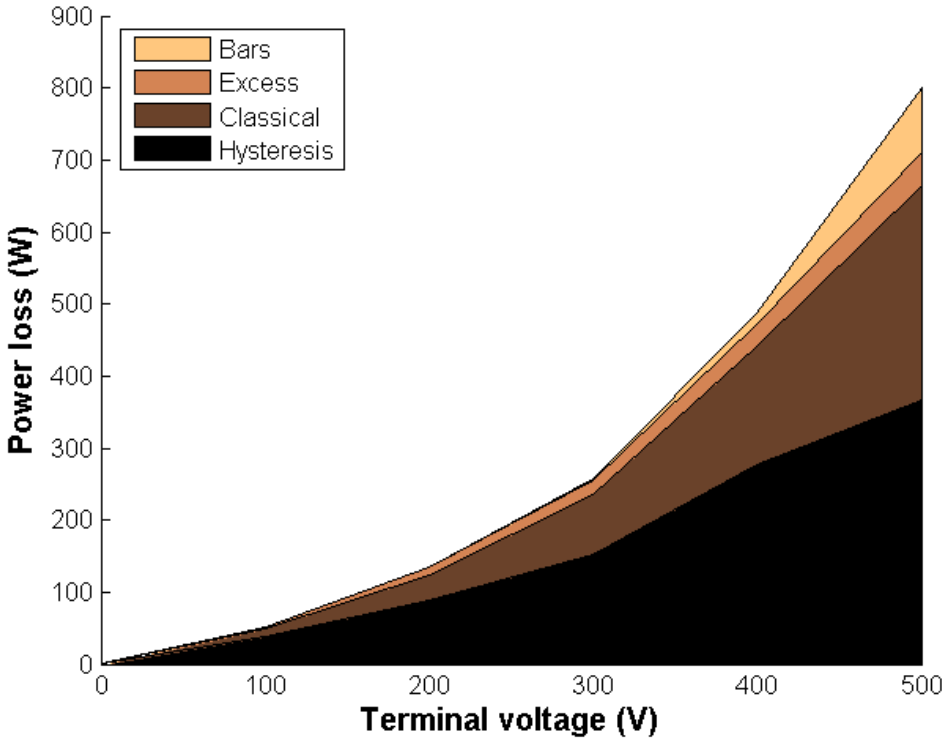

Figure 6 Segregation of the core loss of the induction motor

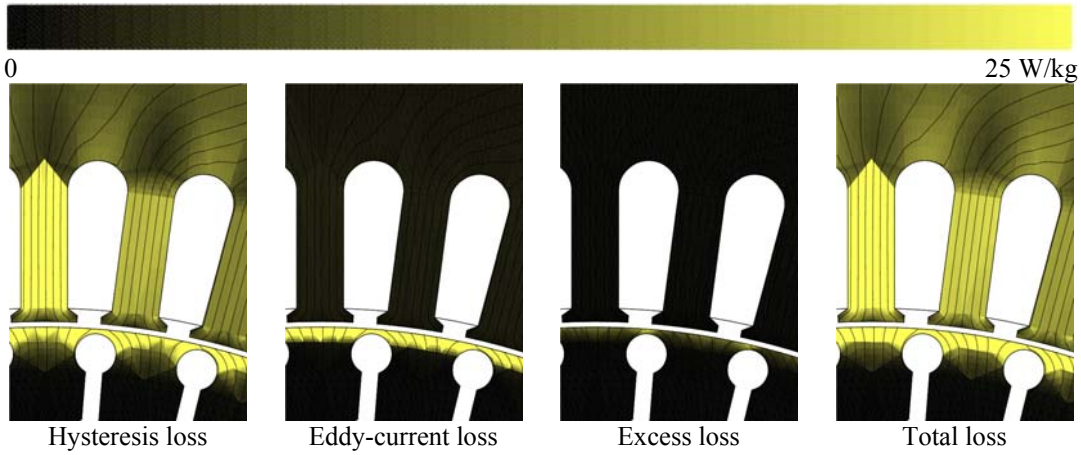

Figure 7 Iron-loss distributions in the induction motor at 400 V

Table 1 Rated data and dimensions of the motor

Shaft power	37 kW
Voltage	400 V
Frequency	50 Hz
Connection	star
Number of pole pairs	2
Stator outer diameter	310 mm
Stator inner diameter	200 mm
Air gap	0.8 mm
Number of stator slots	48
Number of rotor slots	40